LETTER

doi:10.1038/nature14616

A giant protogalactic disk linked to the cosmic web

D. Christopher Martin[1], Mateusz Matuszewski[1], Patrick Morrissey[1], James D. Neill[1], Anna Moore[2], Sebastiano Cantalupo[3], J. Xavier Prochaska[4,5] & Daphne Chang‡

The specifics of how galaxies form from, and are fuelled by, gas from the intergalactic medium remain uncertain. Hydrodynamic simulations suggest that 'cold accretion flows'—relatively cool (temperatures of the order of 10^4 kelvin), unshocked gas streaming along filaments of the cosmic web into dark-matter halos[1–3]—are important. These flows are thought to deposit gas and angular momentum into the circumgalactic medium, creating disk- or ring-like structures that eventually coalesce into galaxies that form at filamentary intersections[4,5]. Recently, a large and luminous filament, consistent with such a cold accretion flow, was discovered near the quasi-stellar object QSO UM287 at redshift 2.279 using narrow-band imaging[6]. Unfortunately, imaging is not sufficient to constrain the physical characteristics of the filament, to determine its kinematics, to explain how it is linked to nearby sources, or to account for its unusual brightness, more than a factor of ten above what is expected for a filament. Here we report a two-dimensional spectroscopic investigation of the emitting structure. We find that the brightest emission region is an extended rotating hydrogen disk with a velocity profile that is characteristic of gas in a dark-matter halo with a mass of 10^{13} solar masses. This giant protogalactic disk appears to be connected to a quiescent filament that may extend beyond the virial radius of the halo. The geometry is strongly suggestive of a cold accretion flow.

We observed the UM287 filament with the Palomar Cosmic Web Imager (PCWI)[7], an integral field spectrograph that is designed for low surface brightness measurements using a $40'' \times 60''$ reflective image slicer with twenty-four $40'' \times 2.5''$ slices. For these observations, the spectrograph covered a range of 3,940–4,110 Å with slit-width-limited resolution $\Delta\lambda \approx 2.5$ Å around the redshifted Lyman-α (Lyα) line. The methodology and details of our observations and data analysis are discussed in the Methods and described extensively elsewhere[8,9]. Data reduction of the PCWI observations resulted in an adaptively smoothed data cube (consisting of the co-added sum of all the exposures) of dimensions right ascension, declination, and wavelength

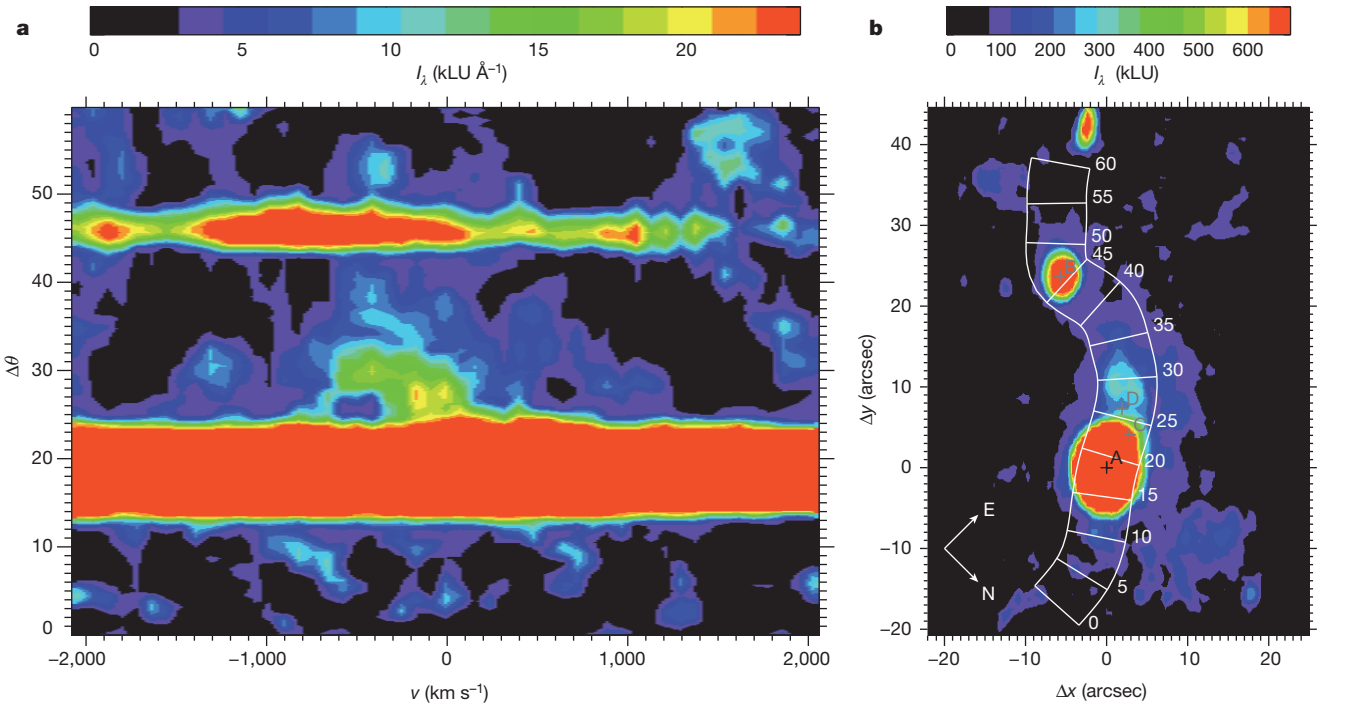

Figure 1 | Spectral image and pseudo-slit spectrum of the QSO UM287 field. **a**, Spectral image of the pseudo-slit (gridded region) in **b**, displayed in velocity with respect to the systemic velocity and arcseconds ($\Delta\theta$) with respect to the reference (QSO source A, which is QSO UM287) position ($z = 2.279$). Flux density I_λ is measured in kilo line units per Å, where 1 kLU Å^{-1} = 1,000 photon cm^{-2} s^{-1} sr^{-1} or 1.18×10^{-19} erg cm^{-2} s^{-1} arcsec^{-2} The signal-to-noise ratio exceeds 7.0. Sources near QSO A are plotted. **b**, Narrow-band image generated from the PCWI data cube by summing the flux density I_λ over the band 3,970–4,000 Å showing the QSO UM287 (source A), the nearby, fainter QSO (source B), and the bright filament of Lyα emission extending from UM287. Emission sources C and D are also shown. The data cube is summed over 7.5 arcsec perpendicular to each position along the pseudo-slit to form the image in **a**.

[1]Cahill Center for Astrophysics, California Institute of Technology, 1216 East California Boulevard, Mail code 278-17, Pasadena, California 91125, USA. [2]Caltech Optical Observatories, Cahill Center for Astrophysics, California Institute of Technology, 1216 East California Boulevard, Mail code 11-17, Pasadena, California 91125, USA. [3]ETH Zurich, Institute for Astronomy, Wolfgang-Pauli-Strasse 27 8093, Zurich, Switzerland. [4]Department of Astronomy and Astrophysics, University of California, 1156 High Street, Santa Cruz, California 95064, USA. [5]University of California Observatories, Lick Observatory, 1156 High Street, Santa Cruz, California 95064, USA.
‡Deceased.

(RA, dec., λ). The bright extended filament is clearly detected in the data (Fig. 1): it is fainter far from QSO UM287 and shows a relatively narrow line (velocity) width (Fig. 1). Channel cuts through the smoothed data cube (Extended Data Figs 2, 4, 5) illustrate a disk morphology, and demonstrate that neither the QSO subtraction nor the presence of a nearby line and continuum object (source C) are responsible for the disk emission that is closest to QSO UM287 (see Methods). To reveal the spatial structure of the emission, we generated a new narrow-band window that follows the velocity-shear structure (Fig. 2).

The narrow-band and spectral images reveal an extended gaseous disk that is offset from, and illuminated by, the nearby quasi-stellar object QSO UM287 (which we call source A). The disk has a diameter of approximately 125 proper kiloparsecs (pkpc), with a central deficit with a diameter of about 25 pkpc. It is inclined by approximately 70° to the plane of the sky. The 2D velocity profile is well fitted by a rotating disk in a Navarro–Frenk–White (NFW) dark-matter halo with mass $\log_{10}M_{\rm h} = 13.1^{+0.6}_{-0.3}$, where $M_{\rm h}$ is the mass of the halo in solar masses ($M_{\odot}$), halo concentration $c = 3^{+5}_{-2}$ (unitless), circular velocity (the maximum rotation velocity of the disk, at the virial radius) $v_{\rm c} \approx 500\,{\rm km\,s^{-1}}$, and virial radius $R_{\rm vir} = 225$ pkpc. Using a pseudo-slit (Fig. 2), we extracted a 1D velocity profile (Fig. 3), which is also well fitted by the same model, with consistent inferred mass $\log_{10}M_{\rm h} = 13.1^{+0.5}_{-0.3}$ and halo concentration $c = 5^{+7}_{-3}$. Both fits include the effects of slit averaging, and the instrument and seeing point spread functions (PSFs) that are measured using QSO A. The velocity profile flattens at the lower end (in detector coordinates), but continues to move blueward slowly at the upper end beyond the disk. The upper end of the disk smoothly transitions into a filament of emission that has a moderate velocity shear of about 100–150 km s^{-1} over a length of at least 125 pkpc. An extended disk of gas provides a natural explanation for the unusual brightness of the QSO UM287 nebula, which when modelled as a cosmic web filament[6] of typical column density required very high clumping factors. The clear disk-like morphology and kinematics of the nebula provide evidence that the Lyα spectral line is probing *in situ* kinematics[10,11].

We model the illumination of the disk by QSO source A and use simple arguments to constrain the geometry (Fig. 4). We assume that this QSO emits symmetrically into two coaxial cones, each with a solid angle of π sr, with the rear cone illuminating the disk, and the front cone including our line of sight. We estimate that under these conditions the QSO can irradiate the disk and filament if the disk is more than 65 pkpc behind the QSO.

We used the 'Cloudy' nebular emission code[12] to model the disk and constrain the gas column density. We find that the gas is optically thin

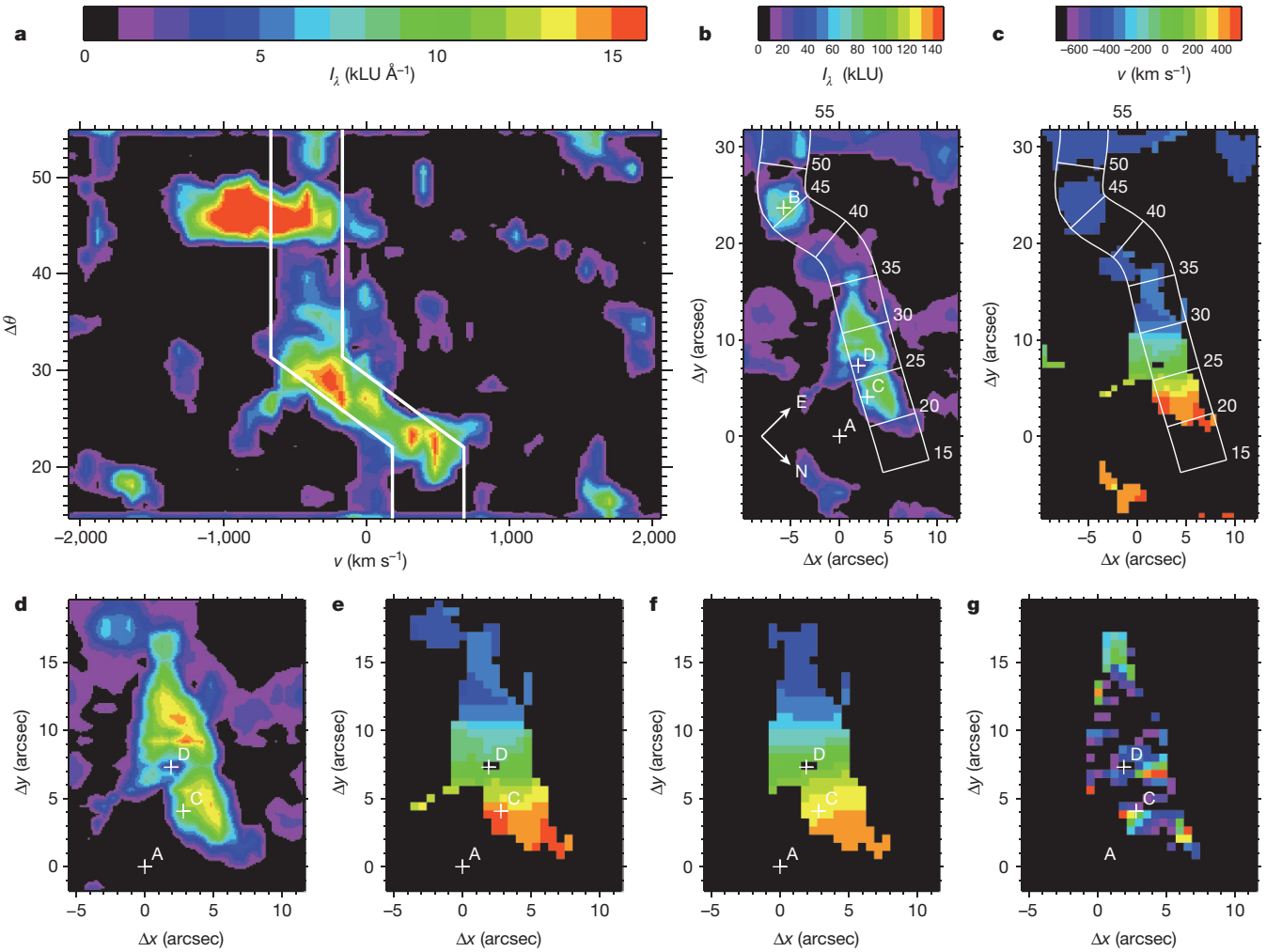

Figure 2 | Spectral image and narrow-band image created from a sheared-velocity window. **a**, Spectral image created with pseudo-slit (gridded region in **b**) and full-field subtraction. v_0 is the systemic velocity of the system. **b**, Narrow-band image formed using sheared, $\Delta v = 500\,{\rm km\,s^{-1}}$ window (bold white lines in **a**). The image and spectrum are consistent with a large (15 arcsec or 125 pkpc), tilted (position angle of 15°), inclined (70°) disk with $v_{\rm c} \approx 450\,{\rm km\,s^{-1}}$ and a central deficit (at gird position (station) 26 arcsec, that is, the grid location along slit). The blueshifted end of the disk transitions to an extended filament. **c**, Mean velocity in the sheared-velocity (kinematic) window (trimmed to show velocities only where emission exceeds 20% of the maximum value). **d**, **e**, Zooms of **b** and **c**, respectively. **f**, 2D velocity model that is compared with **c**. Panel **d** has the same colour scale as **b** and panels **e** and **f** have the same colour scale as **c**. **g**, χ^2 map of the 2D model fit residuals; full-scale $\chi^2 = 5$.

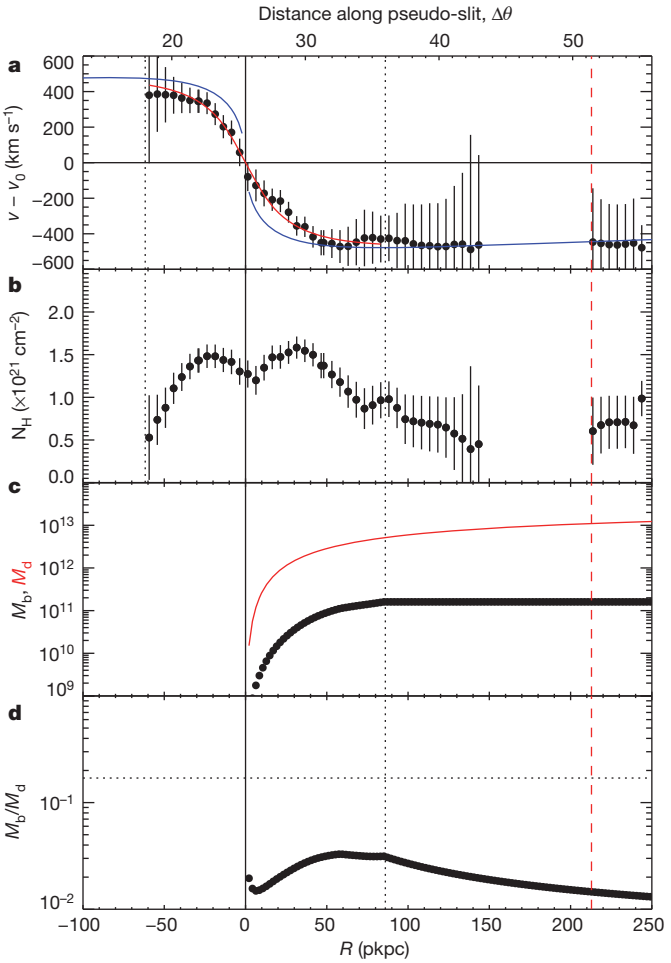

Figure 3 | Physical properties of the extended disk. **a**, Mean velocity (symbols) along the pseudo-slit (Fig. 2) with respect to the disk central velocity v_0, with vertical lines showing an approximately 150 pkpc extent of the disk (dotted black lines), and virial radius (red dashed line). The extent of the filament profile is 80 pkpc $< R <$ 250 pkpc, where R is the radial coordinate of the disk. The NFW profile fits with and without PSF convolution are plotted in red and blue, respectively. Error bars are $\pm 1\sigma$. **b**, Inferred hydrogen column densities N_H assuming $t_d = 3$ pkpc. Error bars are $\pm 1\sigma$ and do not include the uncertainty due to disk thickness. **c**, The cumulative baryonic mass M_b (dots) and dark-matter mass M_d (red line) within a sphere of radius R. **d**, Ratio of baryonic mass inside R to dark-matter mass (symbols) and the canonical ratio of baryonic to dark-matter mass of 0.17 (horizontal dotted line).

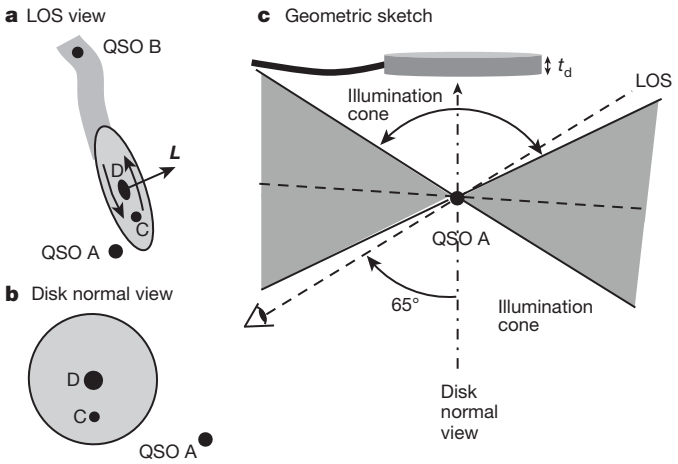

Figure 4 | Sketch of the geometry of the QSO–disk system. **a**, Line of sight (LOS) view as seen by the telescope/PCWI showing both QSOs, the disk, the filament, and the angular momentum vector for the disk, L. **b**, View normal to the disk, for the case of a 125-pkpc distance between QSO A and the disk. **c**, Approximate geometry (showing the QSO, the LOS, the QSO illumination cones (60° half-angle, π sr per cone), for the case of a 125-pkcp distance between QSO A and the disk.

in the Lyman continuum, and that the column density is a strong function of disk thickness and flux only, as previously shown[13,14]. The brightness of the fluorescent Lyα emission suggests that the dust-to-gas ratio in the disk is low (implying low metallicity), because a substantial reduction in output flux at a hydrogen column density $N_H \approx 10^{21}$ cm^{-2} occurs at dust-to-gas ratios greater than 10^{-3}–10^{-2} times the standard Milky Way ratio[15].

Because the inferred gas mass is proportional to the square root of the disk thickness t_d, we require an estimate of t_d. For a self-gravitating gas disk supported by thermal or turbulent pressure, the thickness is related to the gas temperature and column density: $t_d \approx 0.35\left(\frac{T_d}{10^4\,\mathrm{K}}\right)\left(\frac{N_H}{10^{21}\,\mathrm{cm}^{-2}}\right)^{-1}$ pkpc. For all the models in our parameter grid, the disk temperature $T_d \approx 3 \times 10^4$ K, which implies a disk thickness of at least 1 pkpc and a plausible disk gas density $n_H \approx 0.5 t_d^{-0.48}$ cm^{-3}. Simulations that produce extended disks[4] suggest a thickness that is less than 10 pkpc. Such a disk would have three times the column density of the 1-pkpc case and require turbulent velocity support to maintain the 10-pkpc thickness of $\sigma_v \approx 60$ km s^{-1} (for a pressure-supported disk $t_d \approx 5\left(\frac{\sigma_v}{50\,\mathrm{km\,s}^{-1}}\right)^2\left(\frac{N_H}{10^{21}\,\mathrm{cm}^{-2}}\right)^{-1}$), which is comparable to the velocity dispersions in high-redshift disks and is less than the approximately 80–90 km s^{-1} range that would produce efficient shocking and radiative cooling. Additionally, the presence of a clear emission deficit in the central 25 pkpc suggests that the disk is much thinner than 25cos(70°) ≈ 8.6 pkpc. Consequently, we take 1–10 pkpc as a reasonable range and use $t_d = 3$ pkpc for all the mass estimates below, which have errors of ±0.25 dex. We infer the column density as a function of disk radius, assuming a 3-pkpc-thick disk (Fig. 3b).

The estimates above allow us to compare the halo mass profile derived from the rotation fits to the inferred baryonic gas mass profile (Fig. 3c, d). We find that the total baryonic mass in the disk is $M_b = 10^{11.2}\left(\frac{t_d}{3\,\mathrm{pkpc}}\right)^{0.52} M_\odot$, where $M_\odot$ is the solar mass. The ratio of baryonic mass to total mass is $0.013\left(\frac{t_d}{3\,\mathrm{pkpc}}\right)^{0.52}$, which for $t_d = 3$ pkpc is about 8% of the canonical ratio 0.17. As expected, the baryonic mass is about 8% of the baryonic Tully–Fisher relation[16] for $v_c = 470$ km s^{-1}. The low baryon fraction in the cold disk component may imply that either the baryons are lagging the dark-matter collapse or that a substantial component is shocked to a much higher virial temperature. However, the mass profiles in Fig. 3c, d are quite similar, with only a small additional deficit in the inferred baryon ratio at the centre of the disk. We estimate that the filament has a mass $M_{fil} \approx 10^{11} M_\odot$, which is comparable to the disk mass, and suggests that some of the baryons associated with the halo will accrete in the future.

The integral field spectroscopic data allows us also to determine the total angular momentum of the disk baryons: $L_b \approx 3.2 \times 10^{15} t_d^{0.52} M_\odot$ kpc km s^{-1}. The specific angular momentum j_b is independent of the disk thickness: $j_b = L_b/M_b = 2 \times 10^4$ pkpc km s^{-1}. These quantities, in conjunction with the halo parameters, allow us to determine the normalized spin parameter[17]: $\lambda_b = j_b/\left(\sqrt{2} R_{vir} v_{vir}\right) = 0.14$, where v_{vir} is the virial velocity. Typically, dark-matter halos have spin parameters $\lambda_d \approx 0.04$ at $z = 0$, although spin parameters are predicted to be higher at $z = 2$, sometimes reaching[5] $\lambda_d \approx 0.1$. The baryonic spin parameter that we measure is an additional 40% larger, suggesting that the baryons in the extended disk have an angular momentum that is much greater than that of the dark matter halo. The large diameter and very high angular momentum of the structure strongly suggest that the extended disk is a 'cold flow disk', similar to those predicted by simulations[4]. This is the first directly imaged example of such an object, to our knowledge.

The extended disk of QSO UM287 does not have a detected stellar component in the continuum image, although there is continuum emission in the central part of the disk that coincides with the Lyα emission deficit (source D, another bright continuum emission object, is located almost exactly at the centre of the disk). The column density that we estimate, $N_{\rm H} \approx 2.5 \times 10^{21}\,{\rm cm}^{-2}$, is above the star-formation threshold for solar metallicity. Although feedback from the QSO illumination could halt star formation for 1–10 Myr, the continuum rest-frame far-ultraviolet emission probes a 100-Myr timescale. The lack of star formation in the extended disk could be explained by a low metallicity ($Z < 0.1$), which raises the star-formation threshold, owing to the lower dust content and H_2-formation rate[18]. Source D implies a central star-formation rate of $>15 M_{\odot}\ {\rm yr}^{-1}$; the Lyα emission deficit could be caused either by increased dust absorption or by a gas deficit. The central deficit could also be produced by preferential photoevaporation by the QSO, or H I in the foreground (on the observer's side of the QSO) given that H I is abundant in the circumgalactic medium around quasars[19].

Other possible causes of the observed velocity shear deserve comment, such as whether the extended disk is a result of the interactions that produced QSO source A and another bright object, QSO source B. We explore some alternatives in the Methods. QSO-merging disk models and observations imply, in general, a late appearance of the optical QSO phenomenon and only faint and fading signs of interactions. The large size, smooth kinematics and excellent fit to a simple disk model are not consistent with merging disks and tidal tails. The lack of any direct connection to QSO A or velocity shear nearing and crossing QSO B suggest that these objects are not directly linked or fed by the disk. The observations are best explained by an extended rotating disk linked to a cosmic web filament.

Online Content Methods, along with any additional Extended Data display items and Source Data, are available in the online version of the paper; references unique to these sections appear only in the online paper.

Received 18 February; accepted 21 May 2015.
Published online 5 August 2015.

1. Birnboim, Y. & Dekel, A. Virial shocks in galactic haloes? *Mon. Not. R. Astron. Soc.* **345,** 349–364 (2003).
2. Dekel, A. & Birnboim, Y. Galaxy bimodality due to cold flows and shock heating. *Mon. Not. R. Astron. Soc.* **368,** 2–20 (2006).
3. Kereš, D., Katz, N., Weinberg, D. H. & Davé, R. How do galaxies get their gas? *Mon. Not. R. Astron. Soc.* **363,** 2–28 (2005).
4. Stewart, K. *et al.* Orbiting circumgalactic gas as a signature of cosmological accretion. *Astrophys. J.* **738,** 39 (2011).
5. Stewart, K. R. *et al.* Angular momentum acquisition in galaxy halos. *Astrophys. J.* **769,** 74 (2013).
6. Cantalupo, S., Arrigoni-Battaia, F., Prochaska, J. X., Hennawi, J. F. & Madau, P. A cosmic web filament revealed in Lyman-α emission around a luminous high-redshift quasar. *Nature* **506,** 63–66 (2014).
7. Matuszewski, M. *et al.* The Cosmic Web Imager: an integral field spectrograph for the Hale telescope at Palomar Observatory: instrument design and first results. In *Proc. SPIE, Ground-based and Airborne Instrumentation for Astronomy III* (eds McLean, I. S. *et al.*) 77350P (SPIE, 2010).
8. Martin, D. C. *et al.* Intergalactic medium emission observations with the Cosmic Web Imager. I. The circum-QSO medium of QSO 1549+19, and evidence for a filamentary gas inflow. *Astrophys. J.* **786,** 106 (2014).
9. Martin, D. C. *et al.* Intergalactic medium emission observations with the Cosmic Web Imager. II. Discovery of extended, kinematically linked emission around SSA22 Lyα blob 2. *Astrophys. J.* **786,** 107 (2014).
10. Prescott, M. K. M. *et al.* Resolving the galaxies within a giant Lyα nebula: witnessing the formation of a galaxy group? *Astrophys. J.* **752,** 86 (2012).
11. Prescott, M. K. M., Martin, C. L. & Dey, A. Spatially resolved gas kinematics within a Lyα nebula: evidence for large-scale rotation. *Astrophys. J.* **799,** 62 (2015).
12. Ferland, G. J. *et al.* The 2013 release of Cloudy. *Rev. Mex. Astron. Astrofis.* **49,** 137–163 (2013).
13. Bertoldi, F. The photoevaporation of interstellar clouds. I. Radiation-driven implosion. *Astrophys. J.* **346,** 735–755 (1989).
14. Hennawi, J. F. & Prochaska, J. X. Quasars probing quasars. IV. Joint constraints on the circumgalactic medium from absorption and emission. *Astrophys. J.* **766,** 58 (2013).
15. Neufeld, D. A. The transfer of resonance-line radiation in static astrophysical media. *Astrophys. J.* **350,** 216–241 (1990).
16. McGaugh, S. S., Schombert, J. M., de Blok, W. J. G. & Zagursky, M. J. The baryon content of cosmic structures. *Astrophys. J.* **708,** L14–L17 (2010).
17. Bullock, J. S. *et al.* A universal angular momentum profile for galactic halos. *Astrophys. J.* **555,** 240–257 (2001).
18. Krumholz, M. R., McKee, C. F. & Tumlinson, J. The star formation law in atomic and molecular gas. *Astrophys. J.* **699,** 850–856 (2009).
19. Prochaska, J. X. *et al.* Quasars probing quasars. VI. Excess H I absorption within one proper Mpc of $z \sim 2$ quasars. *Astrophys. J.* **776,** 136 (2013).

Acknowledgements We thank T. Tombrello and S. Kulkarni for their support of PCWI. This work was supported by the National Science Foundation and the California Institute of Technology.

Author Contributions D.C.M. is the principal investigator of PCWI, led the observations and analysis of UM287, and was principal author on the paper. M.M., D.C., and P.M. designed, constructed, and operated PCWI. A.M. was the project and technical manager (2006–2010). J.D.N., M.M., and D.C.M. developed the PCWI/KCWI data pipeline and produced the final data cubes. M.M., P.M., S.C., and J.X.P. contributed Keck data and helped edit the paper.

Author Information Reprints and permissions information is available at www.nature.com/reprints. The authors declare no competing financial interests. Readers are welcome to comment on the online version of the paper. Correspondence and requests for materials should be addressed to D.C.M. (cmartin@srl.caltech.edu).

METHODS

Instrument and observations. We have constructed an integral field spectrograph, called the Palomar Cosmic Web Imager (PCWI), that is designed to search for, map, and characterize intergalactic-medium emission and other low surface brightness phenomena[7]. It is built with a $40'' \times 60''$ reflective image slicer with twenty-four $40'' \times 2.5''$ slices. PCWI is mounted at the Cassegrain focus of the Hale 5-m telescope on Mt Palomar, USA. The imaging resolution, while limited by the 2.5″ slicer sampling, can be effectively improved to approximately 1.3″ by dithering the field between individual exposures. A description of the instrument, general observing approach, and data analysis methodology is given in refs 8 and 9. For the UM287 observation, the spectrograph was fitted with a Richardson reflection grating, blazed near 5,000 Å, and has an instantaneous bandwidth of approximately 170 Å with the nod-and-shuffle mask in place. With this grating, the spectrograph attains a slit-limited resolution $\Delta\lambda \approx 2.5$ Å and a peak efficiency of about 4% at 4,000 Å including the telescope and atmosphere.

We obtained a total of 2 h on-source and 2 h off-source exposure centred on QSO UM287 on 23 September 2014. Individual exposures were acquired using the nod-and-shuffle technique[20–22]. The PCWI implementation of nod-and-shuffle uses the central third of the charge-coupled device (CCD) to record the spectrum, and masks the outer two thirds of the detector for storage (restricting the effective common bandpass to about 170 Å given the image slicer offset brick wall pattern and slit curvature). Individual exposure frames are created by interleaving an integral number, N, of on-target telescope pointings of length t with $N+1$ background pointings, the first and last of length $t/2$, and the remainder of length t. This cadence results in separate source and background tiles being built up on the CCD, each equivalent to an $(N \times t)$ exposure. A typical 40-min exposure ($t = 120$ s, $N = 10$; 20 min source and 20 min background) takes approximately 50 min of wall-clock time, including CCD read-out. The benefits of using the nod-and-shuffle method are that the sky is sampled frequently and nearly contemporaneously with the object, it is imaged through the same optical path as the object, and it is recorded using the same detector pixels as the object. This improves sky subtraction precision, reduces the contribution of detector read noise by decreasing the number of CCD read-outs, and limits the impact of instrument systematics. Pixel binning the detector 2 by 2 further reduces the impact of the three-electron (root mean square) read noise.

Data cube generation. We collected numerous calibration images using internal and dome lamps throughout the observing period. The obtained 2D spectra were processed with the PCWI/Keck CWI data reduction pipeline. They were rectified and aligned using geometric mask calibration images and arc lamp spectra. Background panels were subtracted from source panels. Individual 3D data cubes were then wavelength-shifted to compensate for the <1 Å of total flexure using sky lines. The final mosaicked and co-added data cubes were assembled using the astrometry on the basis of the QSO position. The reconstruction is accurate to about 0.5 arcsec (root mean square).

Exposure maps were generated by processing normalized flat-field images (calibration and twilight flats) in a similar fashion. The result is a set of data cubes (RA, dec., and λ) for each exposure, sampled at (0.55″, 1.1 Å) and covering 3,940–4,110 Å. As the nod-and-shuffle mask does not physically contact the CCD, a small amount of diffuse continuum light scatters underneath it and remains in the subtracted cube (<1%). This residual is easily subtracted with a low-order continuum fit. The data cube was normalized using the measured signal from the QSO UM287 and its measured spectrum at 4,000 Å from the Sloan Digital Sky Survey. The absolute flux measurements are accurate to ±10%.

The data cube projections (other than Extended Data Fig. 1a–d) are produced from this difference flux cube by a 3D adaptive-smoothing-in-λ algorithm, which incorporates a hierarchical adaptive-smoothing algorithm in space and wavelength[8,9]. The 3σ noise threshold used for this algorithm is derived directly from the difference cube, and is consistent with the predicted Poisson noise. Raw spectral and narrow-band images compare well with the smoothed images (Extended Data Fig. 1, Fig. 1).

Channel maps. As the filament approaches QSO UM287 (Fig. 1) the mean velocity shears red-ward and the dispersion broadens. A succession of 2-Å channel cuts through the smoothed data cube (Extended Data Fig. 2) illustrate a disk morphology with emission moving linearly towards the QSO (but offset) as the channels move from blue to red. These images also demonstrate that neither the QSO subtraction nor the presence of a nearby line and continuum object (source C) are responsible for the disk emission nearest QSO UM287. To reveal the spatial structure of the emission, we use the kinematic and spatial behaviour gleaned from the channel maps (Extended Data Fig. 2) to design a new narrow-band window that follows the velocity-shear structure. Using this technique we find evidence of an extended gaseous disk offset from, and illuminated by, the nearby QSO (Fig. 3).

Bright QSO subtraction. We generated several figures in the text (Fig. 3, Extended Data Figs 2 and 5) by subtracting an average image. In the case of spectral images, we calculated and then subtracted an average intensity versus slit position map. That is, we calculated a single flux at each slit position and then subtracted it from the spectral image—this can be thought of as a single-value continuum subtraction. In the case of narrow-band images, a single PSF is calculated by averaging over a wavelength range. This average image is subtracted from each narrow-band image. The wavelength range used is 3,958–4,013 Å, and includes the Lyα emission region (we include this to be conservative since it subtracts a small amount of extended emission, but we note it does not noticeably alter the results). In Extended Data Fig. 2, we subtract only the emission within an elliptical contour (reflecting the PSF) near the bright QSO. In Fig. 2, we subtract the average over the full spectral image in order to remove both QSOs and highlight the disk emission. For the narrow-band images in Extended Data Fig. 2 and Fig. 2, we calculate an average image for the bright QSO and subtract that from the narrow-band image, to highlight the disk emission.

Nearby sources and source-subtraction residuals. It is important to demonstrate that the disk emission is not an artefact produced by the nearby QSO or the continuum source C. We show (Extended Data Fig. 3) the CWI, W. M. Keck Observatory narrow-band, and Keck V-band continuum image, along with locations of the QSOs (A and B) and two sources near QSO A (C and D). Source C is a fairly bright, compact continuum and line source near the QSO. Source D is a fainter, slightly extended continuum and Lyα line source also near the QSO. Sources C and D appear distinct in both the Keck continuum and the narrow-band images. Source D falls exactly in the disk emission minimum and centre. Source C is offset north from the centre of the disk (Fig. 2). Residuals following the elliptical contour are outside the subtraction area. When we perform no subtraction (Extended Data Fig. 4), we see that the excess emission associated with the disk and source C are still present in all channels, and in particular in the positive velocity channels. We can also remove the average emission from each entire image, not just near QSO A (Extended Data Fig. 5). Again the average is taken over the range 3,958–4,013 Å including the Lyα emission region. Source C is removed because it is a continuum source, except in the channels in which its line emission appears (Extended Data Fig. 5j, k). Considerable positive-velocity disk emission remains after removing the continuum, particularly in Extended Data Fig. 5h–j, k, and clearly exceeds any small remaining residuals due to small (around 1%) variations of the PSF with wavelength. This emission is well offset from source C. Finally, we can use a stepped vertical pseudo-slit to show a kinematically sheared profile that is consistent with a disk at several locations on and off QSO A (Extended Data Fig. 6).

Kinematic modelling. We model the 2D velocity profile (Fig. 2c, e) with a Navarro–Frenk–White (NFW) dark-matter halo profile[23]. We assume that the velocity profile is circular and dominated by dark matter with no stellar or baryonic contribution. We convolve the predicted 2D profile with the measured PSF based on the QSO A image. The 2D velocity profile is well fitted (Fig. 2f, g) by a rotating disk in an NFW dark-matter halo with mass $\log_{10}M_{\rm h} = 13.1^{+0.6}_{-0.3}$, halo concentration $c = 3^{+5}_{-2}$, central velocity near systemic ($v_0 = 50 \pm 30\,{\rm km\,s^{-1}}$), circular velocity (at the virial radius) $v_{\rm c} \approx 500\,{\rm km\,s^{-1}}$, and virial radius $R_{\rm vir} = 225$ pkpc. Using a pseudo-slit (Fig. 2) we extracted a 1D velocity profile (Fig. 3a), which is also well fitted by an NFW model with consistent inferred geometry, mass $\log_{10}M_{\rm h} = 13.1^{+0.5}_{-0.3}$, and halo concentration $c = 5^{+7}_{-3}$. The blue-shifted end of the disk ($v \approx -450\,{\rm km\,s^{-1}}$) smoothly transitions to an extended filament (80 pkpc $< R <$ 250 pkpc, crossing the faint QSO) with the same velocity of about $-450\,{\rm km\,s^{-1}}$.

Intensity modelling. To constrain the geometry of the disk with respect to the LOS and the QSO, we set up a simple model (Fig. 4). We assume that the QSO has two opposite emission cones each with π sr (60° cone half-angle). The line of sight is included in one of these cones, and the disk and the filament feeding the disk are included in the other. The disk inclination is estimated from the axis ratio and the 2D kinematic model fit to be about $70^\circ \pm 5^\circ$. The requirement that the rear emission cone illuminates all of the visible disk and filament places a lower limit on the separation between the disk and the QSO of 65 pkpc. We note that QSO B could also produce some of the illumination, but we neglect that here.

We use the 'Cloudy'[12] nebular emission code (version 11.10) to estimate the column density and constrain the gas density of the illuminated disk. We use a standard QSO spectrum with luminosity $\log_{10}(\nu L_\nu) = 46.9$, black-body temperature $T = 1.5 \times 10^5$ K, and power-law indices $\alpha_{\rm oX} = -1.4$ (for optical-to-X-ray), $\alpha_{\rm UV} = -0.5$ (for UV), and $\alpha_{\rm x} = -1.0$ (for X-ray). We populate a grid of fixed number density models with total gas column density $\log_{10}N_{\rm H} = \{20.5, 20.6, \ldots, 22.5\}$, distance between the disk and QSO A $r_0 = \{75, 125, \ldots 275\}$ pkpc, disk thickness $t_{\rm d} = \{1, 3, 10, 30\}$ pkpc, disk turbulent velocity $\sigma_v = \{0, 300\}\,{\rm km\,s^{-1}}$, disk metallicity $[Z/H] = \{0, -1, -2\}$. For each of these models a Lyα flux is calculated, with contributions from recombination radiation, line scattering, and collisional excitation also determined. We find that the model predicts that intensity only strongly depends on disk thickness (disk density) and hydrogen column

density, as expected, since the neutral fraction (n_{H^0}/n_H) scales as the square root of the gas density. The model predicts that the gas is optically thin in the Lyman continuum, and thus column density only a strongly depends on disk thickness and flux, as previously shown[13,14]. For recombination radiation we expect $N_H \approx (It_d)^{0.5}$ cm^{-2}where I is the intensity; the resulting model nearly replicates this dependence: $N_H = 10^{21.15} t_d^{0.52} f_0^{0.56} R_{100}^{0.09} \sigma_v^{0.07} [Z/H]^{-0.006}$, where f_0 is the Lyα flux in units of 3×10^{-17} erg cm^{-2} s^{-1} arcsec^{-2} and R_{100} is the distance between the QSO and the disk in units of 100 kpc. The neutral hydrogen column density $N_{H\,I}$ is relatively independent of disk thickness, and varies strongly with QSO/disk separation, ranging from $N_{H\,I} = 10^{16.2}$ cm^{-2} for $R_{100} = 0.75$ to $N_{H\,I} = 10^{17.0}$ cm^{-2} for $R_{100} = 2.0$. In the regime determined from the data, the neutral fraction is low ($\ll$1) and most of the Lyα emission is produced by radiative recombination (as opposed to line scattering[8,24] or collisional excitation[25]). The model is insensitive to whether the disk is thermally or turbulently supported, because, in the model grid, the thickness and column density are fixed to enable us to derive the intensity, and the line emissivity is only a weak function of the turbulent velocity σ_v.

The brightness of the fluorescent Lyα suggests that the dust-to-gas ratio in the disk is low, because substantial reduction in output flux at $N_H \approx 10^{21}$ cm^{-2} occurs with dust-to-gas ratios greater than 10^{-3}–10^{-2} times the standard Milky Way ratio[15]. Finally, we use the average intensity at each point of the pseudo-slit in Fig. 2 to determine N_H as a function of the other parameters. We estimate the filament mass using the same model. Here, the filament thickness is taken to be 24 pkpc, on the basis of a filament width of approximately 3 arcsec, length of 160 pkpc, and a mean $N_H \approx 7 \times 10^{20}$ cm^{-2} (Fig. 3). The filament mass is then $M_{fil} \approx 10^{11} t_{fil}^{0.52} M_\odot$, where $t_{fil} = 24$ pkpc.

We compute the angular momentum of the disk by assuming that the fitted velocity profile (intrinsic, before blurring and averaging) and column density profile apply to the full 180° associated with each half of the disk.

Radiative transfer. Optically thick Lyα radiation can produce a double-peaked profile as line photons escape from the line centre by frequency random walk[15]. The optical depth τ_0 for an H I column density $N_{H\,I} \approx 10^{17}$ cm^{-2} is $\tau_0 \approx 3{,}000$, which for a gas temperature $T \approx 10^4$–10^5 K (and equivalent turbulent velocity) gives a double-peak separation less than 1.5 Å. This separation would not be resolved in our observation. Under these conditions, for line photons escaping a relatively kinematically quiet disk ($\sigma_v < 50$ km s^{-1}), and because we do not expect substantial velocity shears along the line of sight, the line centroid should reflect the average local gas velocity[10,11].

Alternative models. Since the UM287 disk is found in proximity to QSO A (and B), it is possible that it was produced by the same interactions that produced QSO A (and possibly B), or in interactions by the halo that the object could share with QSO A (and possibly B). Simulations of tidal tails in cold dark matter models suggest that long tails can be formed of about 250 pkpc[26–28]. Here we make some general observations, and in this discussion refer to the UM287 nebula as being composed of the bright filament (Fig. 2, at station 20–35 arcsec) and the faint filament (Fig. 2, station 35–50 arcsec). Luminous QSOs at high redshift are probably formed from major mergers of two gas-rich disks[29]. The optical QSO phase is late in the evolutionary sequence of such a merger and tends to show only faded and faint evidence of interactions such as tidal tails[29–34]. Our kinematic observations of the UM287 nebula are well fitted by a smooth rotating disk connected to a quiescent filament with low velocity shear. The intensity distribution is also disk-like. The inferred gas column densities ($10^{21.5}$ cm^{-2}) and gas masses ($10^{11} M_\odot$) are high. The span of the bright filament is 120 pkpc and of the entire filament is several hundred proper kiloparsecs.

We consider three classes of alternative models. First, an undetected disk could be interacting with the host of QSO B, leading to a merging disk and long tidal tails illuminated by QSO A. However, there is no evidence in Lyα for emission or the complex kinematics of a merging disk at, or near, QSO B. Long tidal tails are usually fairly thin, curved, fade away from the interaction region, and show continuous velocity shear as various parts of the tail expand, rotate, and fall back[35]. Neither the intensity, morphology, nor velocity profiles of the UM287 filament exhibit this behaviour. No emission is seen from an opposing tail.

A second possibility is that the bright part of the filament is part of a merging disk hosting QSO A or the tidal tail, and that the faint filament is part of the tidal tail. Several issues arise with this picture. The bright filament is tangential to QSO A with no detected connection, whereas a tidal tail would be expected to project radially outward and then curve tangentially, all in a plane that includes the host merging disk and QSO A. It is difficult to illuminate the bright filament with QSO A unless their separation is at least 100 pkpc, which is inconsistent with the possibility of the bright filament being part of the merging disks. There is no evidence for complex merging disk/tail kinematics, for example large velocity shears where the tidal tail meets the merging disks, or curvature in velocity–position space of the tail[35]. There are no continuum counterparts (other than D) to the filament, as usually seen in tidal tails. The filament is quite wide (approximately 60 pkpc) compared to observed and modelled tails. Gas moving outward in a tidal tail would be likely to show a kinematic discontinuity with the outer disk rotation curve. Typically, the base of the tail is closer to the systemic velocity of the merging system (as well as the end, with a noticeable curvature in between), because this gas (farthest from the centre of mass at perigalacticon) has suffered a tidal impulse that launches the tidal tail. Although there is no direct way to determine whether the gas in the filament is in-falling from the cosmic web or moving outward in a tidal tail, the lack of this kinematic signature is further (indirect) evidence that the gas is flowing in and smoothly merging with the outer parts of the disk.

A third possibility is that the filament is produced by an interaction that does not produce the QSOs but occurs in the same halo. In this case, the main purpose of positing the interaction is to explain the large size of the filament. Again, the simple and smooth kinematics, the large width, the high gas mass, and the disk-like morphology suggest that this is neither a merging disk system or a tidally disrupted disk passing through the halo of QSO A.

Thus, although we cannot investigate all possible interaction geometries and scenarios here, a merger/tidal scenario is not favoured by our observations.

Code availability. We choose not to make the pipeline code available at this time because it is not fully documented for public use but plan to do so in early 2016.

20. Sembach, K. R. & Tonry, J. L. Accurate sky subtraction of long-slit spectra: velocity dispersions at $\Sigma_V = 24.0$ mag/arcsec^2. *Astron. J.* **112,** 797–805 (1996).
21. Glazebrook, K. & Bland-Hawthorn, J. Microslit nod-shuffle spectroscopy: a technique for achieving very high densities of spectra. *Publ. Astron. Soc. Pacif.* **113,** 197–214 (2001).
22. Cuillandre, J. C. *et al.* "Va-et-Vient" spectroscopy: a new mode for faint object CCD spectroscopy with very large telescopes. *Astron. Astrophys.* **281,** 603–612 (1994).
23. Navarro, J. F., Frenk, C. S. & White, S. D. M. A universal density profile from hierarchical clustering. *Astrophys. J.* **490,** 493–508 (1997).
24. Cantalupo, S., Porciani, C., Lilly, S. J. & Miniati, F. Fluorescent Lyα emission from the high-redshift intergalactic medium. *Astrophys. J.* **628,** 61–75 (2005).
25. Cantalupo, S., Porciani, C. & Lilly, S. J. Mapping neutral hydrogen during reionization with the Lyα emission from quasar ionization fronts. *Astrophys. J.* **672,** 48–58 (2008).
26. Barnes, J. E. Encounters of disk/halo galaxies. *Astrophys. J.* **331,** 699–717 (1988).
27. Springel, V. & White, S. D. M. Tidal tailspin cold dark matter cosmologies. *Mon. Not. R. Astron. Soc.* **307,** 162–178 (1999).
28. Toomre, A. & Toomre, J. Galactic bridges and tails. *Astrophys. J.* **178,** 623–666 (1972).
29. Hopkins, P. F., Hernquist, L., Cox, T. J. & Kereš, D. A cosmological framework for the co-evolution of quasars, supermassive black holes, and elliptical galaxies. I. Galaxy mergers and quasar activity. *Astrophys. J.* **175** (Suppl.), 356–389 (2008).
30. Guyon, O., Sanders, D. B. & Stockton, A. Near-infrared adaptive optics imaging of QSO host galaxies. *Astrophys. J.* **166** (Suppl.), 89–127 (2006).
31. Hutchings, J. B. Host galaxies of $z \sim 4.7$ quasars. *Astron. J.* **125,** 1053–1059 (2003).
32. Hutchings, J. B., Cherniawsky, A., Cutri, R. M. & Nelson, B. O. Host galaxies of two micron all sky survey-selected QSOs at redshift over 0.3. *Astron. J.* **131,** 680–685 (2006).
33. Kawakatu, N., Anabuki, N., Nagao, T., Umemura, M. & Nakagawa, T. Type I ultraluminous infrared galaxies: transition stage from ULIRGs to QSOs. *Astrophys. J.* **637,** 104–113 (2006).
34. Urrutia, T., Lacy, M. & Becker, R. H. Evidence for quasar activity triggered by galaxy mergers in *HST* observations of dust-reddened quasars. *Astrophys. J.* **674,** 80–96 (2008).
35. Hibbard, J. E., van der Hulst, J. M., Barnes, J. E. & Rich, R. M. High-resolution H I mapping of NGC 4038/39 ("The Antennae") and its tidal dwarf galaxy candidates. *Astron. J.* **122,** 2969–2992 (2001).

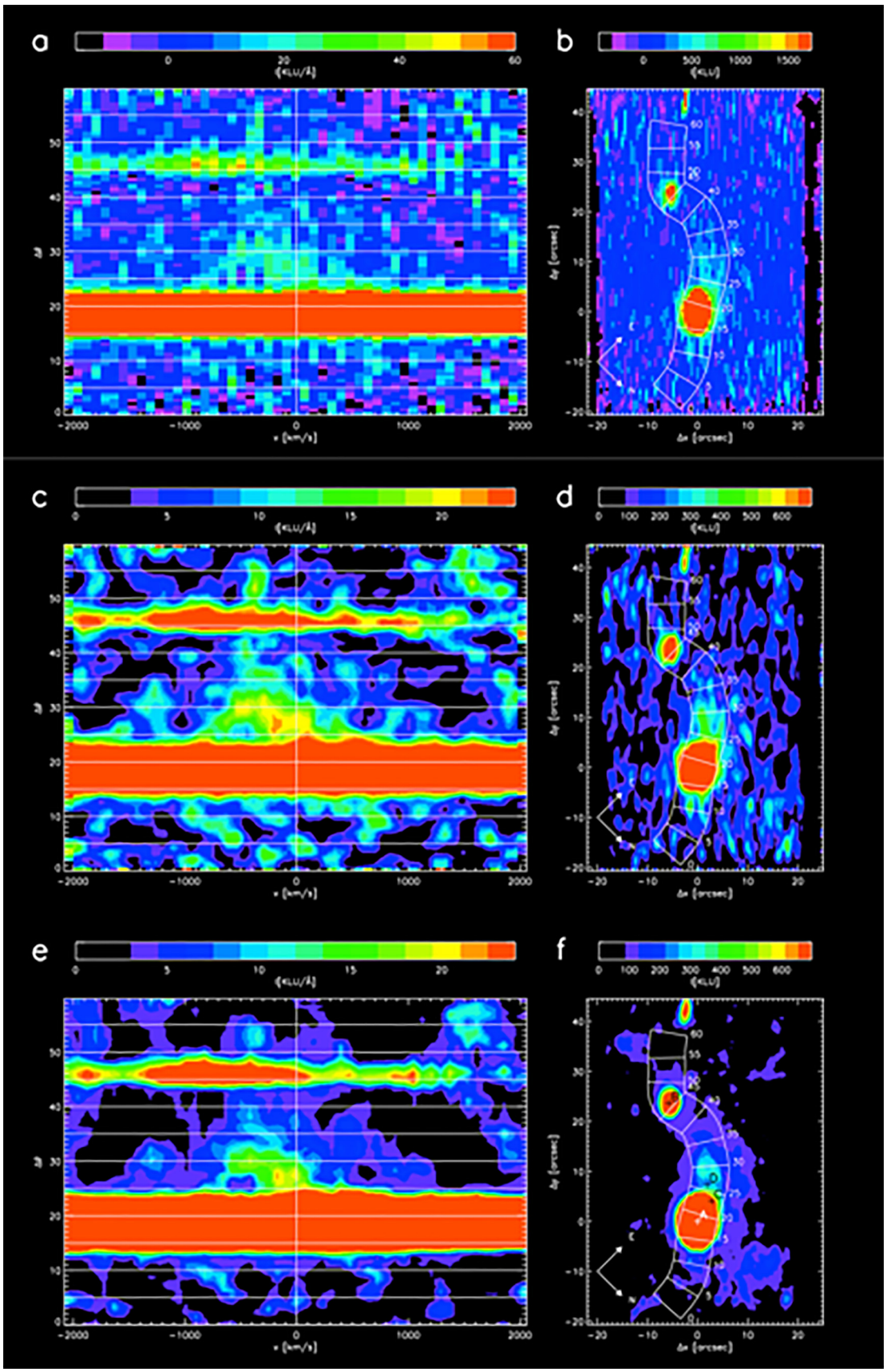

Extended Data Figure 1 | Illustration of raw and conventionally smoothed data. **a**, Raw-data spectral image of pseudo-slit obtained in the slit shown in **b**. 1σ error is about 3 kLU or approximately one colour scale step. **b**, Raw-data narrow-band image obtained in the 3,970–4,000 Å band. 1σ error is 50 kLU or about 0.5 colour scale steps. **c**, Raw spectral image shown in **a**, conventionally boxcar smoothed by 10 pixels. **d**, Raw narrow-band image shown in **b**, conventionally boxcar smoothed by 10 pixels. **e**, Spectral image obtained by 3D adaptive smoothing as discussed in the Methods. **f**, Narrow-band image (3,970–4,000 Å) obtained by summing over the 3D adaptively smoothed data cube, as discussed in the Methods.

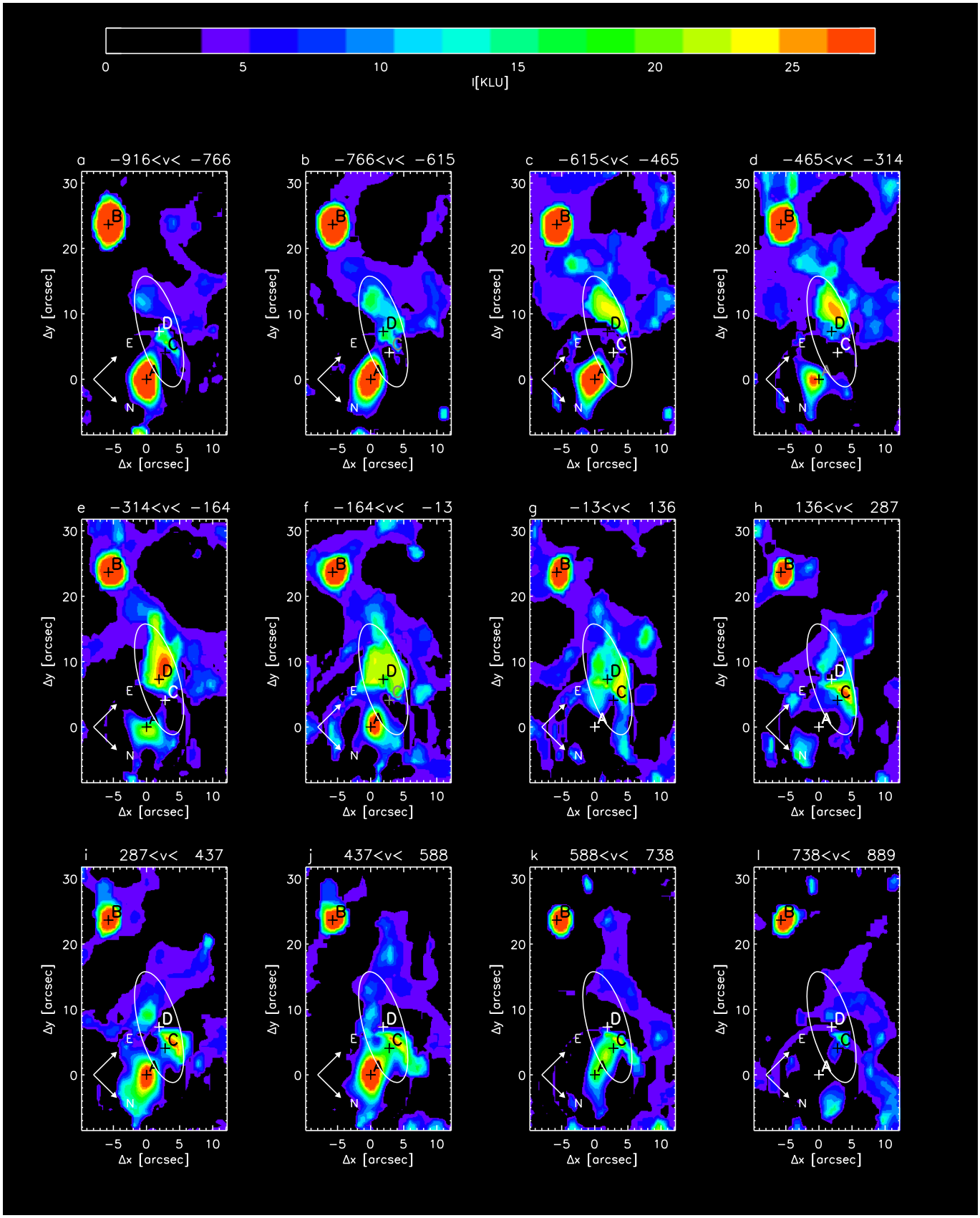

Extended Data Figure 2 | Channel maps of the UM287 data cube. a–l, Panels show individual velocity channels that are 150 km s^{-1} wide, corresponding to a 2 Å width. Sources A–D near QSO UM287 are plotted. Velocities are with respect to the UM287 systemic velocity. QSO A has been subtracted by calculating an average PSF for the QSO over the 3,970–4,000 Å band, and then subtracting this slice by slice, within an elliptical radius of 6 arcsec in the x direction and 7.2 arcsec in the y direction. The residual flux in certain channels is due to three effects. (1) At the centre of QSO A, the residual flux is due to emission lines in the QSO around Lyα. (2) At the elliptical boundary surrounding the QSO, a small subtraction residual can be seen outside the ellipse within which the subtraction is performed. This is typically 3–5 kLU, and can be seen clearly without additional sources in **c** and **d**. (3) Emission sources are present near the QSO in certain channels. Source C shows line emission primarily in **j** and **k** (430 km s^{-1} $< v <$ 731 km s^{-1}), and its continuum emission is subtracted along with the QSO. Any emission near the subtraction boundary above 5 kLU is not a subtraction residual due to the QSO. The disk emission appears bright in **b** southeast of QSO A, and moves north, approaching the QSO as the velocity moves redward. In the two central velocity channels, the emission appears almost ring-like and continues to move north, roughly centred on source D. The emission continues to move north in **h**–**j**. The emission is 15–25 kLU and therefore cannot be QSO subtraction residuals. The emission is also not partially subtracted emission from source C. The emission in **i** and **j** are several arcseconds east of source C. Further evidence for this point is given in Extended Data Figs 4 and 5. To indicate the approximate disk location, we show an elliptical contour with a major axis radius of 8.5 arcsec, position angle of 15.5°, and an ellipticity corresponding to an inclination of 70°.

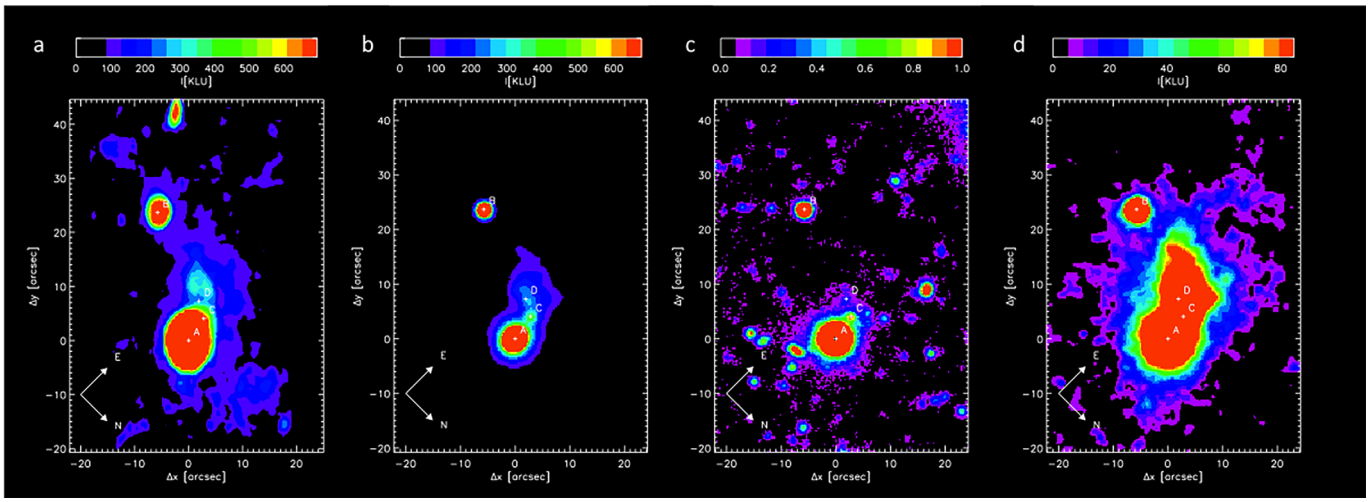

Extended Data Figure 3 | Comparison of PCWI data and Keck narrow-band and continuum images. **a**, PCWI narrow-band image created by summing 3,970–4,000 Å data-cube slices from the adaptively smoothed data cube. Sources A, B, C, and D are shown. PCWI image is not continuum subtracted. **b**, Keck continuum-subtracted narrow-band image on the same intensity scale as the PCWI image in **a**. **c**, Keck V-band image. Sources A, C, and D are shown; continuum magnitudes in the V band are approximately (±2 mag) 16.6 AB, 22.2 AB, and 23.8 AB respectively. **d**, Keck continuum-subtracted narrow-band image on an expanded intensity scale.

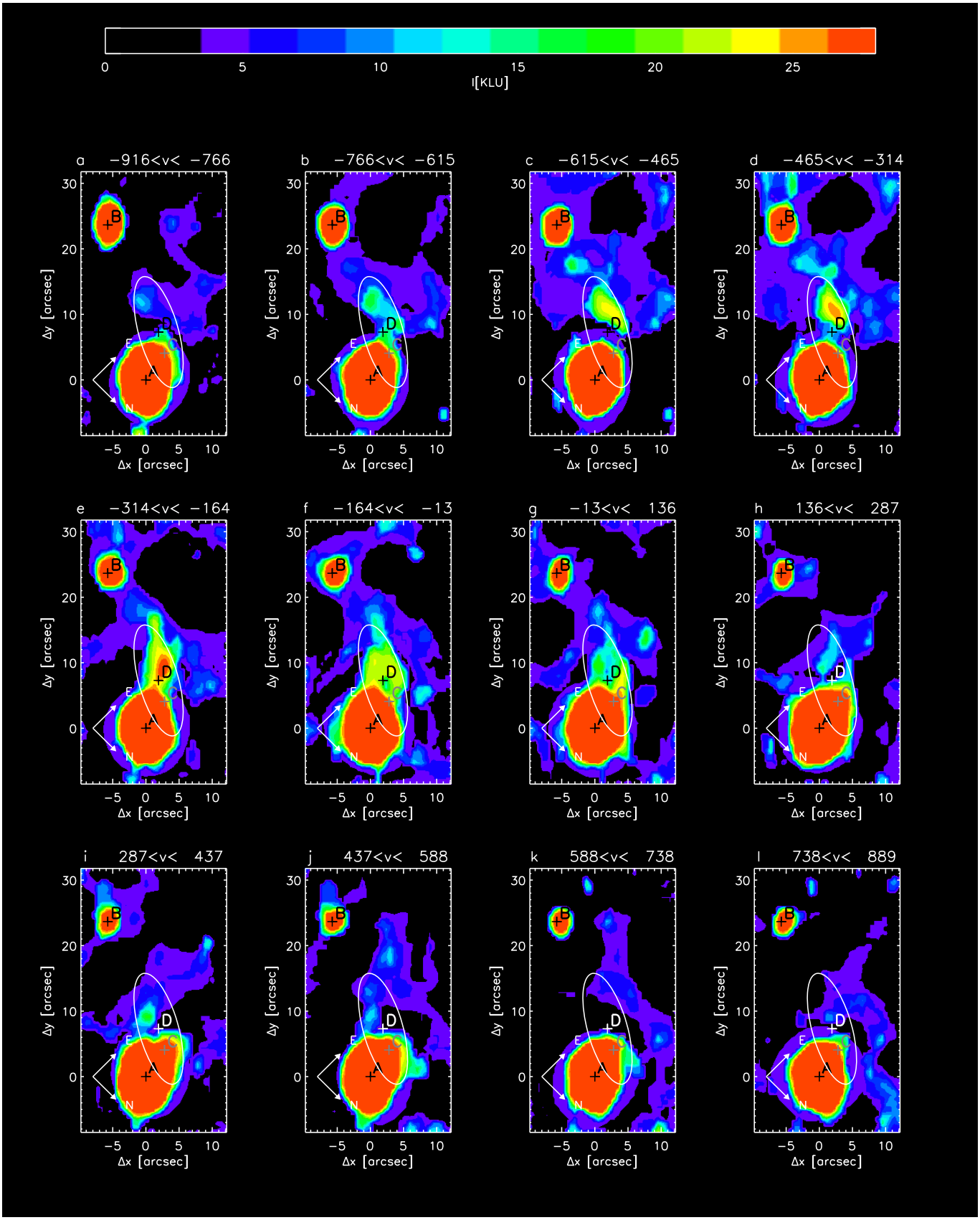

Extended Data Figure 4 | Channel maps of the UM287 data cube. Panels show individual velocity channels that are 150 km s^{-1} wide, corresponding to a 2 Å width, as in Extended Data Fig. 2. In this case, no source subtraction has been performed. Sources near the QSO are plotted. Ellipses are drawn as in Extended Data Fig. 2. Velocities are with respect to the UM287 systemic velocity.

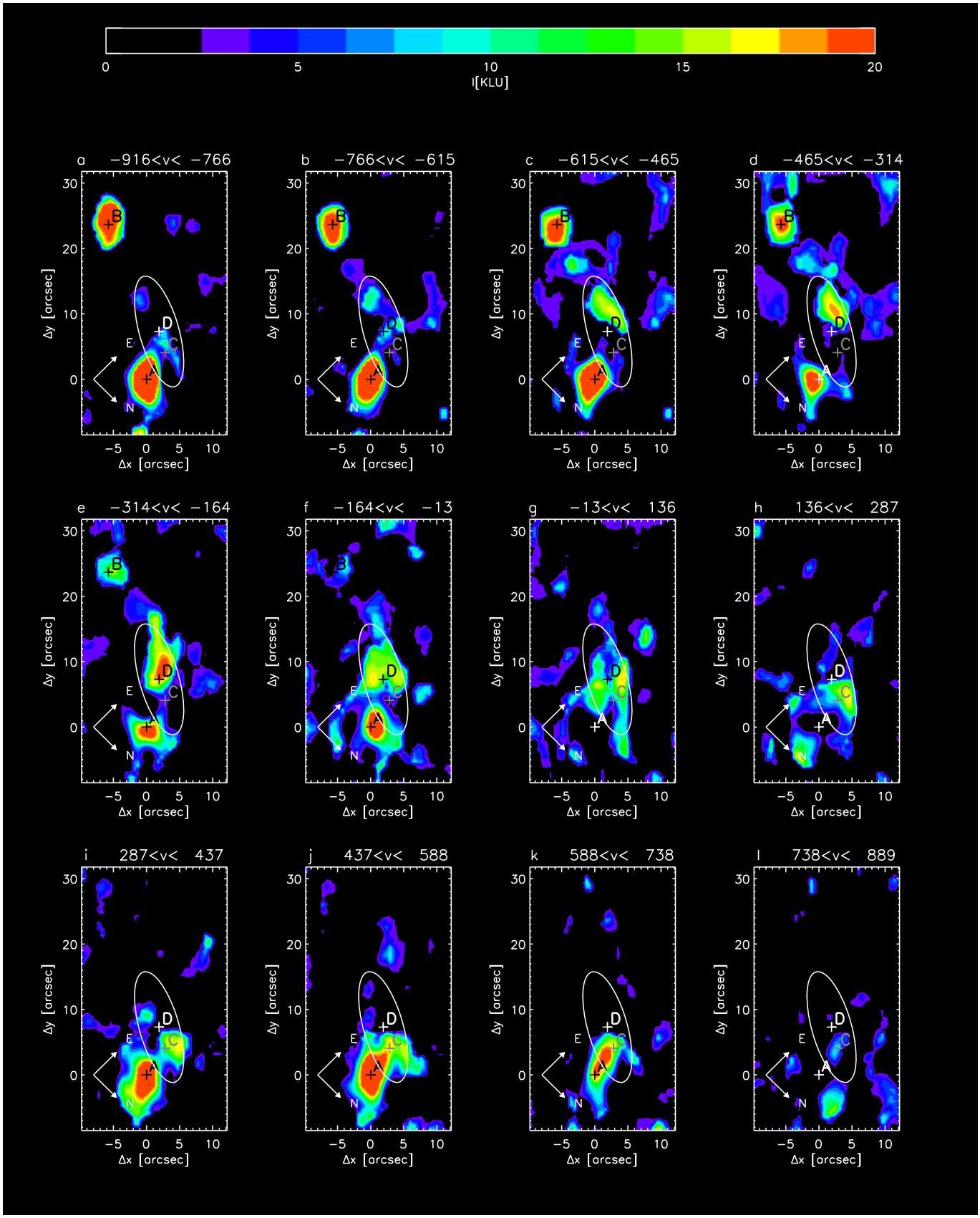

Extended Data Figure 5 | Channel maps of the UM287 data cube. **a–l**, Individual velocity channels that are 150 km s^{-1} wide, corresponding to a 2 Å width, as in Extended Data Fig. 2. In this case, the wavelength-averaged cube has been subtracted from the cube over the full field of view. Sources near the QSO are plotted. Ellipses are drawn as in Extended Data Fig. 2. Velocities are with respect to the UM287 systemic velocity. This subtraction removes the average continuum from all sources, including source C. The emission centred on source C is present in **j** and **k** from line emission (presumably Lyα). The progression of the disk emission can be seen as in Extended Data Fig. 2 from $v = -700$ km s^{-1} to $v = +600$ km s^{-1}.

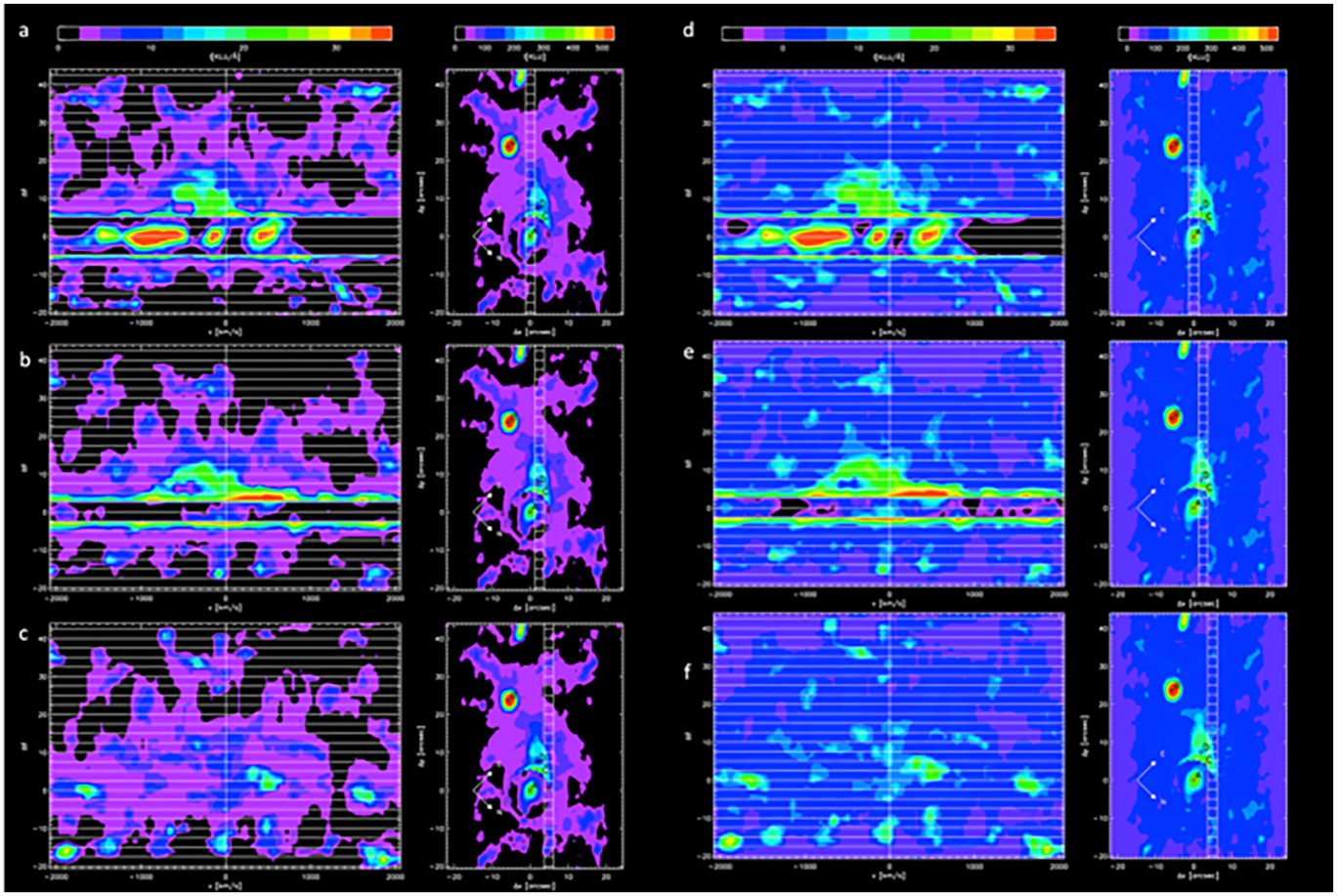

Extended Data Figure 6 | Spectral image and rectangular pseudo-slit slices of the UM287 data cube. **a**–**c**, The spectral image shown at left is in the same format as Fig. 1, and the narrow-band image that is obtained using a $-600\,\mathrm{km\,s^{-1}} < v < 600\,\mathrm{km\,s^{-1}}$ velocity cut is shown on the right with the corresponding slit location from which the spectral image is obtained. The vertical slits are 2.5 arcsec wide, and are positioned at 0 arcsec, 3.75 arcsec, and 5.0 arcsec in the positive x direction (northeast) with respect to the 0 reference position. The average QSO A spectrum has been subtracted in the bright regions. In each spectral image, strong emission appears with a large, quasi-linear velocity shear centred on the QSO velocity. Also, the narrow-band image in this velocity range illustrates that, as the emission approaches the QSO, there is an offset to the northeast that is not consistent with a direct entry into the QSO. **d**–**f**, The same plots with the minimum intensity range set to a negative value to show negative residuals from the QSO subtraction.